Biofabrication

PAPER • **OPEN ACCESS**

Combining rotary wet-spinning biofabrication and electro-mechanical stimulation for the *in vitro* production of functional myo-substitutes

To cite this article: Nehar Celikkin *et al* 2023 *Biofabrication* **15** 045012

IOP Publishing Biofabrication 15 (2023) 045012 https://doi.org/10.1088/1758-5090/ace934

Biofabrication

OPEN ACCESS

RECEIVED
3 February 2023

REVISED
29 May 2023

ACCEPTED FOR PUBLICATION
20 July 2023

PUBLISHED
9 August 2023

PAPER

Combining rotary wet-spinning biofabrication and electro-mechanical stimulation for the *in vitro* production of functional myo-substitutes

Nehar Celikkin[1], Dario Presutti[1], Fabio Maiullari[2,3], Marina Volpi[4], Yurii Promovych[1], Konrad Gizynski[1], Joanna Dolinska[1], Agnieszka Wiśniewska[1], Marcin Opałło[1], Alessia Paradiso[4], Chiara Rinoldi[4], Claudia Fuoco[5], Wojciech Swieszkowski[4], Claudia Bearzi[2,6,7], Roberto Rizzi[2,6,7], Cesare Gargioli[5] and Marco Costantini[1,*]

[1] Institute of Physical Chemistry, Polish Academy of Sciences, Warsaw, Poland
[2] Istituto Nazionale Genetica Molecolare INGM 'Romeo ed Enrica Invernizzi', Milan, Italy
[3] PhD Program in Cellular and Molecular Biology, Department of Biology, University of Rome Tor Vergata, Rome, Italy
[4] Faculty of Materials Science and Engineering, Warsaw University of Technology, Warsaw, Poland
[5] Department of Biology, University of Rome, Tor Vergata, Rome, Italy
[6] Department of Medical Surgical Sciences and Biotechnologies, Sapienza University of Rome, C.so della Repubblica 79, 04100 Latina, Rome, Italy
[7] Institute of Biomedical Technologies, National Research Council of Italy (ITB-CNR), Segrate, Milan, Italy
[*] Author to whom any correspondence should be addressed.

E-mail: mcostantini@ichf.edu.pl

Keywords: 3D bioprinting, skeletal muscle tissue engineering, mechanical stimulation, electrical stimulation, bioreactor

Supplementary material for this article is available online

Abstract

In this work, we present an innovative, high-throughput rotary wet-spinning biofabrication method for manufacturing cellularized constructs composed of highly-aligned hydrogel fibers. The platform is supported by an innovative microfluidic printing head (MPH) bearing a crosslinking bath microtank with a co-axial nozzle placed at the bottom of it for the immediate gelation of extruded core/shell fibers. After a thorough characterization and optimization of the new MPH and the fiber deposition parameters, we demonstrate the suitability of the proposed system for the *in vitro* engineering of functional myo-substitutes. The samples produced through the described approach were first characterized *in vitro* and then used as a substrate to ascertain the effects of electro-mechanical stimulation on myogenic maturation. Of note, we found a characteristic gene expression modulation of fast (MyH1), intermediate (MyH2), and slow (MyH7) twitching myosin heavy chain isoforms, depending on the applied stimulation protocol. This feature should be further investigated in the future to biofabricate engineered myo-substitutes with specific functionalities.

1. Introduction

In our bodies, skeletal muscles (SMs) are responsible for a multitude of key vital functions comprising approximately 40% of total body weight and up to 50%–75% of all body proteins [1]. Alongside their crucial role in motion, SMs are also responsible for glucose, amino acids, and lipids homeostasis. From a structural standpoint, SM tissue owns a particular architecture where the multinucleated fibers are densely packed to form parallelly aligned bundles. Notably, such hierarchical architecture can also be observed at the single cell level in SM cells (SMCs). The organelles in SMCs, in fact, are localized in a highly compact matrix of contractile proteins, and this cellular structure has a major impact on myofiber size, function, form, and localization of the nuclei [1, 2].

Its peculiar characteristics and unique functions place SM tissue at high levels of importance in biomedical research, especially in tissue engineering. In recent years, great efforts have been spent to create

engineered muscle constructs for regenerative medicine purposes, as well as designing functional *in vitro* models for drug testing and musculoskeletal disease investigation [3–7]. To match SM functionality observed *in vivo*, the main focus of these studies has consisted of (i) recapitulating the highly anisotropic architecture of the SM tissue by developing increasingly sophisticated techniques [8, 9] and (ii) identifying physical—i.e., mechanical, electrical or a combination of them—stimulation protocols that could enhance the differentiation levels of SM progenitors [10–13].

Despite the significant technological advances in the field, a proper recapitulation of SM's unique structure and functions still remains a challenge, especially in the case of large volumetric constructs. The scenario is even more complex regarding the identification of physical stimulation protocols to promote the maturation of the engineered muscle constructs. Notably, it has been demonstrated that electrical, mechanical, or electro-mechanical stimuli play a pivotal role in regulating SM cell behavior both in terms of 3D organizations and protein expression [14]. Nevertheless, the underlying mechanisms of such regulation are not completely understood. Moreover, it has still to be determined how to adjust the stimulation protocols to the specific, dynamic features of the engineered muscle constructs (e.g., dimensions, architecture, microenvironment properties, SM cell differentiation level, culturing conditions, etc). This issue has generated literature with contradictory results where electro-mechanical stimuli have induced a significantly improved or even completely inhibited SM maturation [7, 15, 16].

In this context, the rising biofabrication techniques represent a promising option for manufacturing large-volume, standardized engineered SM constructs. Such technologies offer high spatial resolution in terms of biomaterial and cell patterning, together with high repeatability and the possibility to scale up the construct dimension to tens of cm^3 [8, 9]. However, for the majority of available biofabrication platforms, there exists an inverse proportion between printing resolution and printing speed which often limits researchers' manufacturing freedom. In addition, in the specific case of SM constructs, the 3D assembly of volumetric, highly anisotropic structures having high fiber spatial density is not trivial. Here, we present an innovative, fully automated 3D rotary wet-spinning (RoWS) biofabrication strategy that could address these challenges. The presented system offers significant advantages, including high printing speed (typical fiber extrusion rate $\approx$4.2 m min^{-1}, the volume of bioink deposited $\approx$0.5 ml min^{-1}) and capability to manufacture biomimetic, aligned fiber bundles. In addition, we introduce a new microfluidic printing head (MPH) design compatible with the continuous wet-spinning process that enables the production of core/shell hydrogel fibers loaded in the soft core with SM progenitors. After preliminary exploring the system capabilities, we validated the proposed platform through the production of myo-substitutes which were first characterized *in vitro* and then used as a substrate to ascertain the effects of physical stimulation on myogenic maturation, with particular attention to the modulation of the expression of fast and slow twitching myosin heavy chain (MHC) isoforms.

2. Experimental section

Materials: All chemicals were purchased from Sigma-Aldrich and used without further purification unless otherwise stated. Low molecular (LMW-ALG, Mw 33 kDa) and high molecular weight (HMW-ALG, Mw 100 kDa) sodium alginates were kind gifts from FMC Biopolymers. C2C12 myoblasts were kind gifts from the laboratory of Prof. Gargioli. High glucose Dulbecco's essential medium (DMEM), fetal bovine serum (FBS), phosphate buffer solution (PBS), 4-(2-Hydroxyethyl) piperazine-1-ethane sulfonic acid (HEPES) buffer solution, goat serum (GS), trypsin-ethylenediaminetetraacetic acid (EDTA), Alexa Fluor 488 Phalloidin, Texas Red anti-rabbit secondary antibody, were purchased from ThermoFisher (the Netherlands).

2.1. 3D wet-spinning bioprinting setup

Core/shell hydrogel fibers were fabricated and 3D spatially deposited using a custom 3D wet-spinning bioprinter built in our laboratory. The whole platform comprises (i) an extrusion system composed of a 3D printed MPH bearing a crosslinking bath microtank with a co-axial nozzle placed at the bottom of it for the immediate gelation of extruded core/shell fibers (inner needle diameter = outer needle diameter = 500 μm), rotating drum collector (diameter = 20 mm, length = 180 mm), and an X-axis (travel range = 160 mm). The whole system was controlled with an Arduino Mega board and custom software developed in Python. The MPH was designed using Inventor and manufactured through stereolithography 3D printing (DWS 3500PD) using a transparent and class I biocompatible (Class I polymer for surgical guides as per Rule 5, Annex IX of Medical Devices Directive 93/42/EEC) resin (DS3000). After the 3D printing, the nozzle was thoroughly rinsed in isopropanol to remove unreacted photoresin trapped in the channels, dried, and additionally crosslinked in a UV curing oven for another 10 min. Finally, the 3D printed MPH was equipped with a crosslinking bath microtank and mounted on the bioprinter's x-axis arm.

2.2. Simulations of the co-axial flow

The stability of the numerical model was built using COMSOL Multiphysics 5.6 with computational fluid dynamics (CFD) module. The level set method was applied to trace the spatial distribution of two immiscible liquid phases: core and shell. Due to the axial symmetry of the nozzle, the system was modeled in 2D axisymmetric geometry. The symmetry plane was extracted from the source file used for the 3D printing of the nozzle, so it was identical to the experiment. The model was meshed with the standard, physics-controlled mesh calibrated for flow studies. The element size was set to extremely fine, with the minimum and maximum element sizes set to 26.7 nm and 8.71 μm, respectively. The thickness of the interface was set to the default value for the selected mesh. The reinitialization parameter γ was 1 m s^{-1}. The viscosities of the core and shell fluids were set to 15 mPa·s and 80 mPa·s (see figure S1-bface934supp1.pdf), respectively, corresponding to the experimental values. The volumetric flow rates for phases Q_c (core flow rate) and Q_s (shell flow rate) were varied to find the most stable flow conditions. The total time of the simulation was 5 s, with the state of the system recorded every 0.01 s. At every recorded state, the radial position of the interface at the outlet of the nozzle was calculated. Only the simulation's last 2 s were used to analyze the flow's stability since, during the initial part, the flow changed significantly from the initial conditions (see figure S2-bface934supp1.pdf). The stability of the interface was calculated based on the amount of interface from its mean (see SI for more details). A total of 36 independent simulations were performed for values of Q_c and Q_s ranging from 80 and 640 μl min^{-1}.

2.3. C2C12 culture and expansion

C2C12 myoblasts were cultured in high glucose DMEM supplemented with 10% FBS, 1% penicillin-streptomycin, and 10 mM HEPES until 50% confluence was obtained. Further, cells were detached using trypsin-EDTA and encapsulated in the core solution at a final density of 12×10^6 cells ml^{-1}.

2.4. Fabrication of engineered SM constructs

Core/shell hydrogel fibers were fabricated using the custom co-axial MPH. The core bioink was composed of 12×10^6 C2C12 myoblasts/ml suspended in sterile-filtered solution of 1.4% w/v fibrinogen from bovine plasma and 0.2% w/v LMW-ALG in 25 mM HEPES buffer solution containing 150 mM NaCl. The shell biomaterial ink was prepared by dissolving 2% w/v LMW-ALG, 0.5% w/v HMW-ALG, and 0.5% w/v Alginate-RGD (ALG-RGD) in 25 mM HEPES (Alginate RGD synthesis is reported in SI). Prior to use, the MPH and tubing were first washed with 70% ethanol solution and ultimately flushed with sterile dH_2O. The inks were supplied to the MPH nozzle at constant flow rates to generate the co-flow in the extrusion nozzle. In all cellular experiments, typical core and shell flow rates were: $Q_c = 160$ μl min^{-1}, $Q_s = 320$ μl min^{-1}. The crosslinking bath microtank was then filled with 0.6 M $CaCl_2$ solution prior to the extrusion of core and shell inks. The gelation of the core/shell fibers occurs instantaneously in the proximity of the tip of the nozzle upon coming into contact with $CaCl_2$. The resulting hydrogel fiber is initially pulled gently upwards with a tweezer until it reaches the surface of the rotating Teflon drum. As soon as the fiber touches the drum, a hydrogel fiber starts to be continuously extruded from the nozzle and collected onto the drum forming a bundle. The rotation speed of the drum was set to 64 rpm, and the thread number in each bundle was kept constant (37 threads in each bundle, 30 s of extrusion). Following extrusion, the samples were collected from the rotating drum. To crosslink the bioink in the core, the bundles were incubated with 10 U ml^{-1} thrombin in 25 mM HEPES buffer solution for 30 min at 37 °C. The bundles were then separated and immersed in high glucose DMEM, supplemented with 20% FBS, 1% penicillin-streptomycin, and 10 mM HEPES, and cultured at 37 °C in a humidified atmosphere of 5% CO_2 and 95% air for 14 d.

2.5. Electro-mechanical stimulation of SM fascicle

The engineered SM myo-substitutes were either cultured in Petri dishes at their free length or transferred into the bioreactor for physical stimulation. The samples were cultured in high glucose DMEM, supplemented with 20% FBS, 1% penicillin-streptomycin, and 10 mM HEPES over 14 d. Based on other studies present in the literature, four different stimulation protocols (static stretching (SS), dynamic stretching (DS), electrical stimulation (ES), and SS + ES) were selected to determine the effect of physical stimulation on the myogenic maturation of bioprinted samples [3, 6, 17, 18]. The samples were placed in the bioreactor directly after fabrication for SS protocol. The distance between pillars was adjusted to 30 mm and kept constant for 14 d. The DS protocol of the fibers entailed a progressive increase of the stretching amplitude to compensate for the relaxation of the samples upon stretching. The initial distance between the pillars was set to 30 mm, and on day 3, the DS protocol was initiated. The stretching was applied at a speed of 0.5 mm s^{-1} with a 1 s break after each stretch cycle. The stretching length was set at 31.5 mm (5% stretching with respect to the initial length) on day 3, increased to 33 mm (10% stretching) on day 7, and to 36 mm on day 10 (20% stretching). Every day, the myobundles were cyclically stretched for an overall period of 8 h, followed by a 16 h rest period. ES protocol was started on

day 5 of culture when sufficient myotube formation was observed. The ES protocol consisted of 1 h active stimulation followed by 7 h rest period. Electrical impulses delivered to myobundles were bipolar with 70 mA amplitude and 2 ms duration [14]. During ES, myobundles were placed between parallel platinum electrode wires in Petri dishes at their free length. The ES protocol was programmed using a custom pulse generating Labview script combined with a custom electronic board. For SS + ES protocol, the samples were placed in the bioreactor directly after fabrication, and the distance between pillars was adjusted to 30 mm. The platinum electrodes were fixed on the pillars of the bioreactor. The SS and ES protocols were implemented simultaneously with the parameters mentioned above of the single protocols.

2.6. Actin, myosin heavy chain (MHC), laminin (LMN), dystropin (DYS), titin (TTN), and bungarotoxin (BTX) staining

Core/shell bundles were fixed on day 14, and the samples were permeabilized with 0.3% (v/v) Triton X-100 in HEPES. Thereafter, constructs were then incubated in 1% (w/v) bovine serum albumin (BSA) in HEPES overnight at 4 °C to inhibit the non-specific binding. Following the BSA blocking step, the samples were incubated with 1:40 dilution of Alexa Fluor phalloidin in HEPES solution for actin staining. Following the actin staining, samples were washed and subsequently incubated in 1:500 4′,6-diamidino-2-phenylindole (DAPI) solution in HEPES for 10 min. Regarding immunofluorescence stainings, after the samples were fixed with 4% formalin, they were washed with 25 mM HEPES and treated with saturated solution of EDTA containing 0.08% (w/v) alginase for 3 h at 37 °C. Then, the samples were washed with 25 mM HEPES and treated with 0.3% (v/v) Triton X100 solution for permeabilization. After washing the Triton solution with 25 mM HEPES, the samples were blocked with 1%(w/v) BSA in 25 mM HEPES containing 0.08% alginase for 2 h at 37 °C. Subsequently, the scaffolds were incubated with: Anti-Myosin (Skeletal) antibody (MF 20 was deposited to the DSHB by Fischman, D.A. (DSHB Hybridoma Product MF 20)) produced in mouse (1:1), Anti-Laminin (Sigma L9393) produced in rabbit (1:50), Anti-Titin (Abcam ab-284 860) produced in rabbit (1:100), Anti-Dystrophin (Vector VP-D508) produced in mouse (1:100) overnight at 4 °C. After washing, the constructs were incubated with secondary antibody produced in goat (1:500) for 3 h at room temperature (RT): Alexafluor 555 anti-mouse (1:1000), Alexafluor 488 anti-rabbit (1:1000), Texas Red anti-rabbit (1:1000). Subsequently, cell nuclei were stained with DAPI solution (1:500) for 10 min, Bungarotoxin conjugated with Alexafluor 488 was added with DAPI (1:500). After washing, the cell-laden constructs were imaged under confocal microscope (Nikon, A1R). The directionality of the myofibers was performed using image analysis software (ImageJ, National Institutes of Health, USA).

2.7. Quantitative real-time polymerase chain reaction (qRT-PCR) analysis for myosin heavy chain genes (MyH)

Total RNA was extracted from the samples of each experimental condition. The spun samples were washed in 25 mM HEPES for 10 min, transferred in a 2 ml RNase-free Eppendorf tube, quickly frozen in dry ice, and stored at −80 °C until RNA extraction process. The RNA extraction from samples was performed using the pestle and mortar procedure. The mortar, pestle, and spatulas were previously cooled using liquid nitrogen for optimal results. Then, the sample was transferred into the mortar using the spatula and finely ground with the pestle. During the procedure, a small amount of liquid nitrogen was poured into the mortar, preventing the sample's thawing. Subsequently, 1 ml of TRIzol reagent (Invitrogen, Life Technologies) was used to collect the pulverized sample and transferred in a 1 ml RNAse-free new Eppendorf tube. The collected samples were incubated for 5 min at RT to allow complete dissociation of nucleoprotein complexes. The 0.2 ml of chloroform per ml of TRIzol was added to each sample. Tubes were vigorously shaken for 15 s, incubated at RT for 3 min, and centrifuged at 12 000 × g for 15 min at 4 °C. The aqueous phase was transferred to a fresh tube, and RNA was precipitated with 0.5 ml of isopropyl alcohol. After centrifugation, the RNA pellet was washed with 1 ml of 75% ethanol and centrifuged at 7500 × g for 5 min at 4 °C. Finally, the RNA pellet was air-dried and dissolved in 10 μl of RNAse-free water. RNA concentration was determined using a NanoDrop UV–visible spectrophotometer. The 0.5 μg of total RNA was reverse transcribed to cDNA using the High-Capacity cDNA Reverse Transcription Kit (Applied Biosystem, Foster City, California, USA). The evaluation of gene expression was performed by qRT-PCR using 7900HT Fast Real-time PCR System equipped with SDS software (Applied Biosystems) and specific primers for myosin heavy chain 1 (MyH1), myosin heavy chain 2 (MyH2) and myosin heavy chain 7 (MyH7) genes (table 1). All reactions were performed in 10 μl reaction volume and in duplicate. The expression data were normalized using the Ct values of the housekeeping mouse gene GAPDH. The fold changes of each target gene compared to the non-stimulated control group were evaluated.

2.8. Statistical analysis

All measurements were made in triplicates on at least three different samples produced from different cell

Table 1. Murine primer sequences used for qRT-PCR analysis.

Gene symbol	Sense-forward primer	Antisense-reverse primer
MyH1	TGCAATCAAAGGTCAAGGCC	ATCTTGCGGAATTTGGCCAG
MyH2	AAGTAAAGGCCAAGAACGCG	CTCCTCCTCGTACTGTTCCC
MyH7	TACTCTGACCAAGGCCAAGG	CACCTTCTTCTCCTGCTCCA
GAPDH	TCCACTCATGGCAAATTCAA	TTTGATGTTAGTGGGGTCTCG

culture batches and tested independently. Data are reported as mean values ± standard deviation. One-way analysis of variances (ANOVA) test was performed, and differences were displayed as statistically significant when $p \leqslant 0.05$. Statistically significant values are presented as $^{*}p \leqslant 0.05$, $^{**}p \leqslant 0.01$, $^{***}p \leqslant 0.001$, and $^{****}p \leqslant 0.0001$.

3. Results and discussion

3.1. Design and validation of the 3D RoWS bioprinter and MPH

As the 3D printing technologies progress at a rapid pace, the research in the tissue engineering field started seeking new bioprinters that are compact, user friendly, and focused on more specific applications. Particularly, in recent years, significant efforts have been made to design new bioprinters and scaffold fabrication techniques for tissues requiring specific directionality. In this context, we have developed an innovative biofabrication platform for creating engineered myo-substitutes that was inspired by the wet spinning technique. The designed 3D RoWS printer is composed of three main components: (i) a MPH for fiber extrusion, (ii) a rotating drum for fiber collection, and (iii) an x-axis motion arm for the automated assembly of 3D structures (figure 1(a)). The MPH can be featured as the main component of the 3D RoWS system enabling the continuous production of core/shell hydrogel fibers. As presented in figures 1(b) and (c), the MPH is characterized by two main inlets, one for the fiber core and one for the fiber shell. These two inlets are fluidically connected to the two compartments of a co-axial nozzle where the two bioinks meet each other, forming a core/shell flow pattern. The latter is finally extruded within a crosslinking bath microtank where an instantaneous ionic crosslinking between alginate chains in the shell phase and calcium ions in the bath takes place, thus freezing the core/shell flow arrangements (figure 1(d)). Such design simplifies the continuous production of hydrogel fibers by eliminating the need for additional external crosslinker flow (i.e., multi-axial nozzles), hence reducing the complexity of the fiber formation process [19–21].

Thanks to the durable and flexible support of the alginate shell, the proposed system allows for the confinement of a wide variety of low viscosity bioink cores, including fibrinogen, which would otherwise be impossible to use in 3D bioprinting experiments (figure S1-bface934supp1.pdf). This feature enables the widening of the time window for the crosslinking of the core bioink, hence being compatible with long crosslinking processes (e.g., enzymatic reactions). Fibrinogen hydrogels, with their exceptional biocompatibility, unique viscoelastic properties, and tunable degradation rates, emerge as an outstanding biomaterial for SM engineering. Hence the proposed core–shell bundles support the encapsulation and growth of SMCs, mimic the mechanical properties of native muscle tissue, and allow for gradual scaffold remodeling, promoting integration and maturation of engineered muscle constructs [21–23].

Another advantageous aspect of the proposed 3D rotary wet spinning bioprinter is the possibility to control, in specific ranges, the core and shell dimensions by tuning the flow rates of the two bioinks [24–26]. Nevertheless, the stability of the interface between the core and the shell phases within the extrusion nozzle plays a key role in the extrusion process. Therefore, to gain a deeper understanding of the extrusion process, we have analyzed by means of CFD simulations the shape and the behavior of the interface between the two phases at flow rate regimes (figure 2(a)). For these simulations, we used as input parameters the rheological properties of two bioinks that, based on our prior experience, on the one hand, would be compatible with the very rapid wet-spinning process and, on the other hand, would support a proper differentiation of SM progenitors. Accordingly, we select for the shell phase a 3% w/w alginate solution and for the core a solution containing 14 mg ml^{-1} of fibrinogen and 0.2% w/w LMW-ALG (for more details, see section 2.2). As shown in figure 2(b), the size of the core phase decreases for small values of Q_c and large values of $Q_{s,}$ while, conversely, larger Q_c and smaller Q_s result in a structure with a thicker core and a thinner shell. Regarding the stability of the core/shell flow pattern, the stability of the interface was analyzed for the conditions at which the smoothest structure could be produced. As demonstrated in figure 2(c), the stability of the core/shell flow patterns—measured in terms of interface fluctuations—can be obtained at large values of Q_s (generally, $Q_s > 300$ μl min^{-1}). Furthermore, the highest interface stability was observed at $Q_c = 80$ μl min^{-1}/$Q_s = 640$ μl min^{-1},

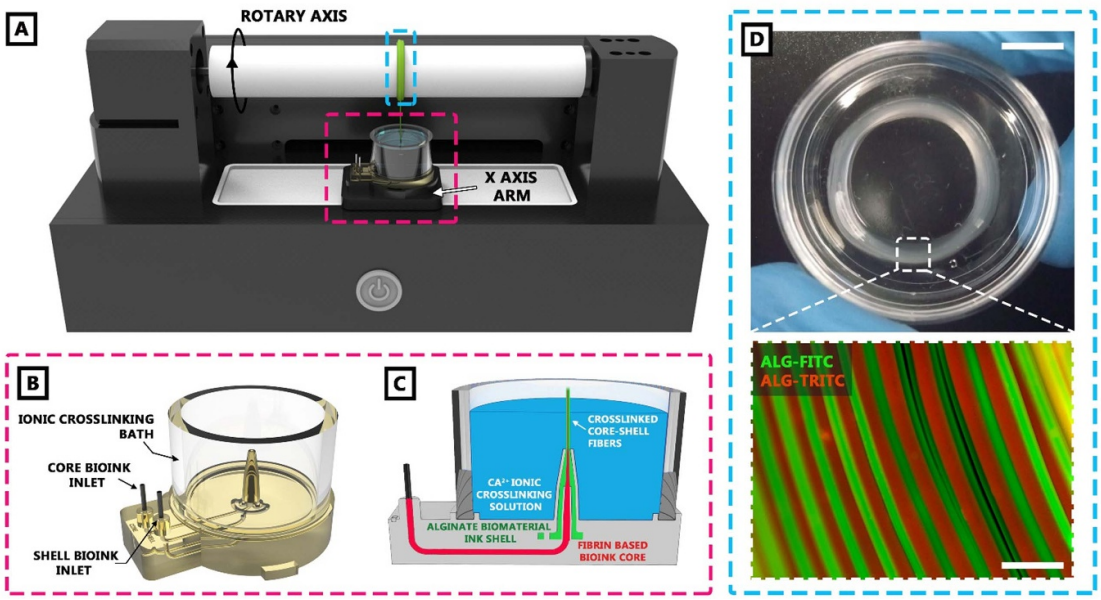

Figure 1. (A) 3D rendering model of the rotary wet-spinning printer (3D RoWS) displayed with its three main components: (i) the microfluidic printing head, (ii) the rotating drum collector, and (iii) the *x*-axis motion arm. (B) Representation of the microfluidic printing head and core/shell inlet channels (C) cross-section of the microfluidic printing head displaying fluidic paths within the MPH. (D) (top) Hydrogel core/shell fiber bundle composed of parallelly aligned fibers. (bottom) Confocal image of the bundle showing the precise organization of fibers and their accurate core/shell structures. Scale bars: (A) overall bioprinter dimensions 310 × 165 × 150 mm; (B), (C) $D_{channels} = 800\ \mu m$, $D_{core} = 500\ \mu m$, $D_{shell} = 500\ \mu m$, $D_{crosslinking\ bath} = 26$ mm; (D) (top) 2 mm, (D) (bottom) 800 μm.

indicating that the shear stress resulting from the velocity difference between the phases stabilizes the flow pattern. These results were of the utmost importance as they helped us to identify the most suitable flow regimes for fiber production, avoiding a time-consuming experimental optimization of these parameters.

Based on CFD results, we experimentally tested our MPH using Q_c and Q_s values from the bottom left quadrant of the heat maps shown in figures 2(b) and (c). The rationale behind this decision is that we wanted to obtain stable core/shell fibers without using too high flow rate values that could be potentially harmful to cells—in terms of shear stresses. We thus selected two different flow rate sets with the same Q_s/Q_c ratio (Q_s:160/Q_c:80 μl min^{-1} and Q_s:320/Q_s:160 μl min^{-1}) to validate the predictions of CFD simulations and evaluate the core/shell fiber characteristic dimensions. For these experiments, we fixed the rotational drum speed to 64 rpm. The results are shown in figures 2(d) and (e). In the first case, with $Q_s = 160\ \mu$l min^{-1} and $Q_c = 80\ \mu$l min^{-1}, we observed a relatively stable fiber extrusion with minor interruptions due to the break-up of the extruded fibers. The overall fiber diameter was 275 ± 23 μm, the core diameter 190 ± 20 μm, and the wall thickness was 43 ± 6 μm. In the second case with doubled values, the overall fiber diameter measured 372 ± 25 μm, the core diameter 236 ± 20 μm, and the wall thickness 68 ± 10 μm. In this case, we did not observe any fiber break up during extrusion, and the continuous extrusion process resulted smooth for the whole spinning procedure.

Interestingly, the soft cores result in partially deformed, being squeezed by the adjacent layers of fibers present in the bundle. Since these results appeared to agree with CFD simulations, we thus chose the second set of flow rate values for the following experiments with cells. Remarkably, the obtained wall thickness values should guarantee a sufficient diffusion of nutrients to the cells encapsulated in the core.

From a structural point of view, a key aspect often desirable in SM tissue engineering (SMTE) is to mimic the anisotropic, aligned architecture of native muscles, possibly at the largest scale. To this aim, the proposed 3D RoWS bioprinter can create hydrogel bundles of parallelly aligned fibers at a speed of approx. 0.5 ml min^{-1} (figure 3(a)). This speed is remarkable considering that in other studies, the fiber deposition speed ranged from approx. 5 μl min^{-1} to 50 μl min^{-1}, thus being up to two orders of magnitude higher [8, 27]. To demonstrate the potential of our systems, we first fabricated onto the rotating drum single-layer bundles containing a different number of fibers by using a constant linear speed in the *x*-axis ($V_{x\text{-axis}} = 30$ mm min^{-1}) and simply tuning the extrusion time (figure 3(b)). The adhesion of extruded fibers to previously collected ones on the drum can be attributed to two effects. Initially, hydrogel fibers adhere to each other due to capillary forces. Once tightly packed, the partially

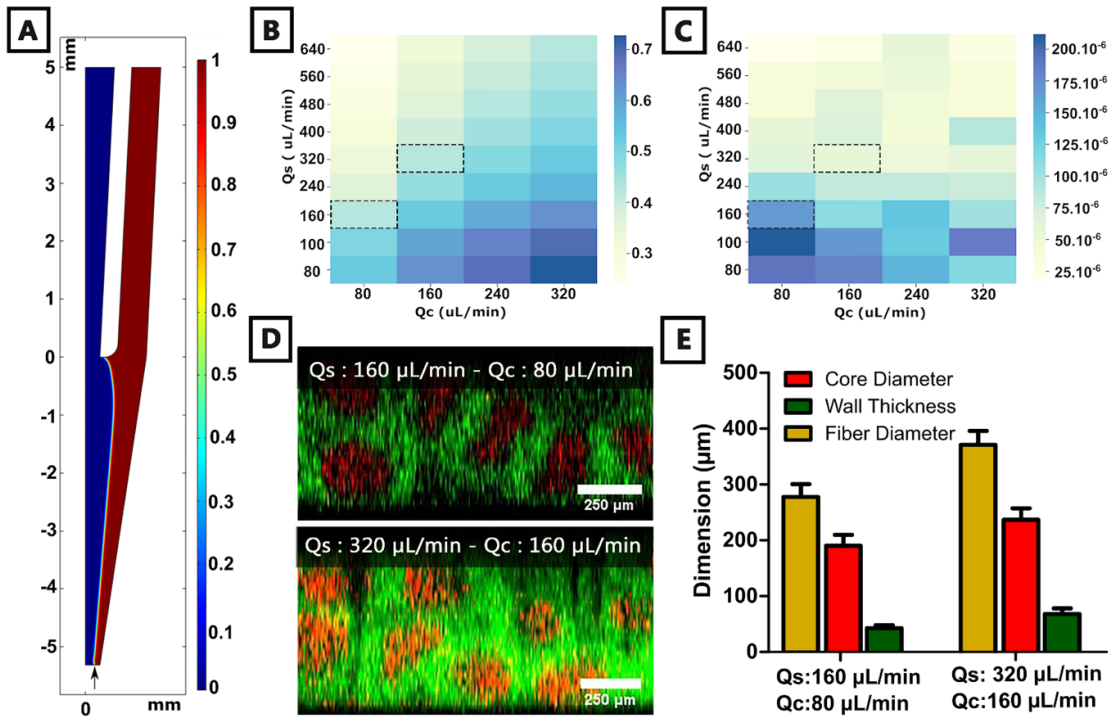

Figure 2. (A) The spatial concentration of core/shell liquids inside the nozzle. Blue and red colors correspond to a high value of the core and shell phase, respectively. The white line between both phases indicates the interface. The point at the outlet of the nozzle at which instabilities of the interface were measured is marked with an arrow. (B) Core-to-shell thickness ratio as the function of the flow rates of both liquids Q_c and Q_s. The flow rates marked with the bright color yield a structure with a thin core and thick shell. The opposite composition of the structure is marked with dark colors. (C) Stability of the interface as the function of the flow rates. The color scale bar represents the amount of interface fluctuations, calculated as the standard deviation of the interface position normalized to nozzle radius (see SI for details). Dark regions indicate a highly unstable regime where the interface position at the nozzle outlet varies significantly in time. The bright rectangles correspond to conditions at which a structure with a smoother interface can be produced (D) Confocal images of core–shell fibers (core: TRITC tagged alginate, shell: FITC tagged alginate) (E) the wall thickness, core diameter, and overall fiber diameter of the core/shell fibers (Q_s:160/Q_c:80 μl min^{-1}, Q_s:320/Q_c:160 μl min^{-1}, respectively, $n = 10$).

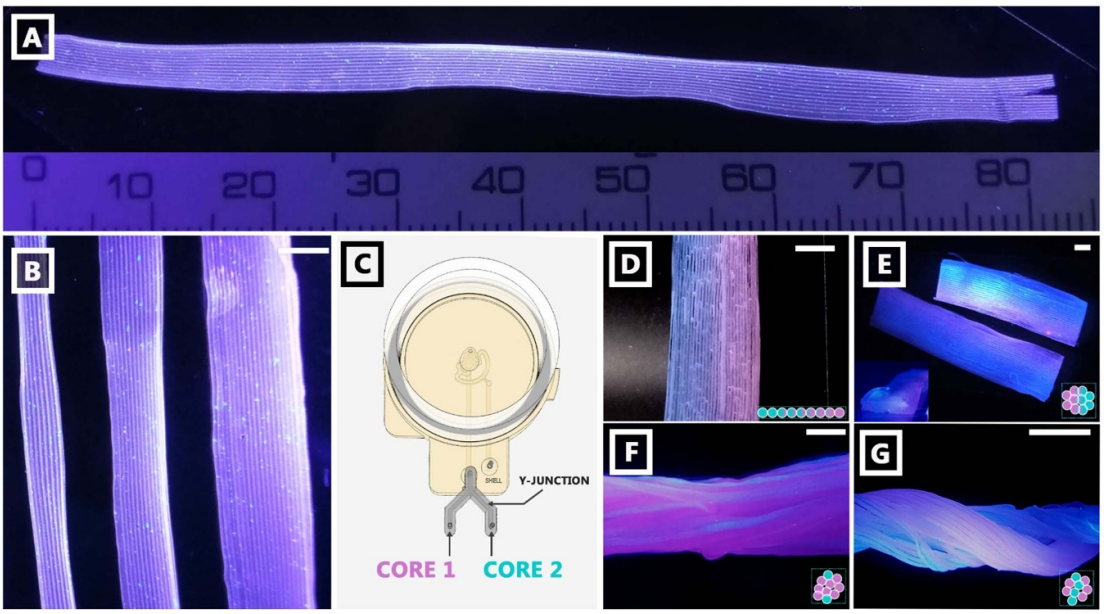

Figure 3. Multi-size and multi-material 3D rotary wet spun core–shell constructs. A single layer core–shell hydrogel bundle's entire length is depicted in (A) and (B) several hydrogel bundles bearing variable numbers of fibers. Representation of the microfluidic printing head with Y-junction installed upstream of the core inlet (C) to fabricate multi-material core extrusion in a single-layered (D) and multi-layered (E) hydrogel bundles, the progressive change from blue to pink indicates the gradual transition between of the core material. (F)–(G) Different multi-layered hydrogel bundles containing varying core material fibers (scales bars: 5 mm).

crosslinked alginateJ shells continue forming the hydrogel network with adjacent fibers. Experimental results support that an extrusion time of approximately 150 ms within the crosslinking bath effectively stabilizes the core/shell architecture, but it is insufficient for the complete crosslinking of the alginate shells. Consequently, when collected onto the drums, the hydrogel fibers, still moist with the crosslinking solution rich in Ca^2+ ions, interact with one another, allowing the alginate chains to form links between adjacent fibers. This aspect is crucial for maintaining the stability of the hydrogel bundle during *in vitro* culture. Additionally, a Y-junction was installed upstream of the core inlet to demonstrate the possibility of fabricating multi-material 3D core/shell bundles (figure 3(c)). By tuning the extrusion flow profiles of the core inks, one can design 3D bundles where, for instance, (i) the spatial core composition is changed gradually (figure 3(d) single layer, figure 3(e) bundle) or (ii) the ratio of fibers having different cores is precisely varied (figures 3(f) and (g)).

These system features may be used for biofabricating cellularized samples characterized, for instance, by graded mechanical properties or containing various ratios of different cell types. Altogether, these characteristics confirm that the proposed 3D RoWS bioprinter represents an ideal platform for the biofabrication of highly aligned soft tissues such as SMs, ligaments, and tendons.

3.2. Biofabrication of engineered SM constructs using 3D RoWS

Matrix stiffness and the presence of cell adherence cues play crucial roles in the spreading, elongation, and cooperative fusion of myoblasts, as well as in myotube maturation [28, 29]. Hence, we paid particular attention to the formulation of the shell and core inks to achieve successful elongation and maturation of myoblasts. As mentioned in the previous paragraph, the shell phase was formulated using alginate as the main component to instantaneously stabilize the core/shell fibers upon extrusion. However, it is well known that alginate, in its pristine form, does not support cell adhesion. We thus decided to chemically modify it using short peptides bearing RGD sequences, a common motif responsible for cell adhesion [30, 31]. We believe, in fact, that ALG-RGD may help in creating a cell adhesive interface between the two fiber compartments where, at first, myoblasts and, later, myotubes may anchor themselves. Regarding the core ink composition, we envisioned that the myoblast-encapsulating matrix should provide both a convenient stiffness for cell elongation/spreading and durable mechanical characteristics to prevent a premature collapse of the core architecture during the myotube maturation and contractions. Amongst the plethora of biomaterials tested for SMTE, without doubt, fibrin has become the gold standard substrate for *in vitro* SM tissue models [15]. Fibrin contains several bioactive sites to interact with cells and growth factors, including fibroblast growth factor-2 (FGF2), vascular endothelial growth factor (VEGF), and insulin-like growth factor-1 (IGF-1), that promote myoblast migration, proliferation, and differentiation [32–34]. Moreover, the fibrinolytic enzymes secreted during muscle differentiation have been proven to promote myoblast fusion, matrix turnover, and tissue remodeling, which may enable improved contractile function [16]. We first formulated a core ink containing only 14 mg ml^{-1} of fibrinogen and 12×10^6 C2C12 cells ml^{-1}. Such ink supported a very rapid myoblast spreading and proliferation (figure 4(a)). However, on day 3 of *in vitro* culture, the majority of the core matrix was already digested by cells, thus leading to the premature collapse and clustering of the neo-forming myotubes. The core composition was enhanced by adding ALG-LMW at a concentration of 2 mg ml^{-1} to overcome such issues. Despite being an inert biomaterial, adding ALG at low concentrations had no significant impact on C2C12 elongation, spreading, and differentiation. The addition of ALG improved the mechanical durability of the core matrix that sufficiently supported the myoblast differentiation and myotube maturation over 14 d. Syncytia formation in the core was observed starting from day 7, and random contractions in the myobundles were recorded between days 10 and 14 (bface934supp2.mp4). Myoblasts in the engineered SM constructs showed a remarkable muscle differentiation demonstrated by significant MHC expression and an average myotube thickness of 15 ± 3.3 μm (figures 4(b) and (c)). The myoblast fusion allows the addition of new myonuclei to the growing syncytium, which contributes to sustained and harmonious muscle growth. Moreover, confocal image analysis indicated a pronounced alignment of the cells and neo-myofibers during tissue maturation along the fiber axis, confirming that the selected core/shell architecture and composition effectively guided tissue maturation. Muscle progenitors were spatially confined in a soft, cell-friendly and -adhesive fibrinogen core surrounded by a stiff, inert alginate shell; accordingly, the shell acted as a physical barrier, thus confining cells in the core. The highly anisotropic architecture of the core, with their length being significantly larger than that of their diameters, can also be considered as the major driving force for an efficient differentiation along the major axis of the fibers. Additionally, the relatively high flow rate for the extrusion of the core/shell fibers most likely induces the polymer chains in the inks to undergo a shear/induced preferential orientation, thus contributing to the anisotropy of the system down to the

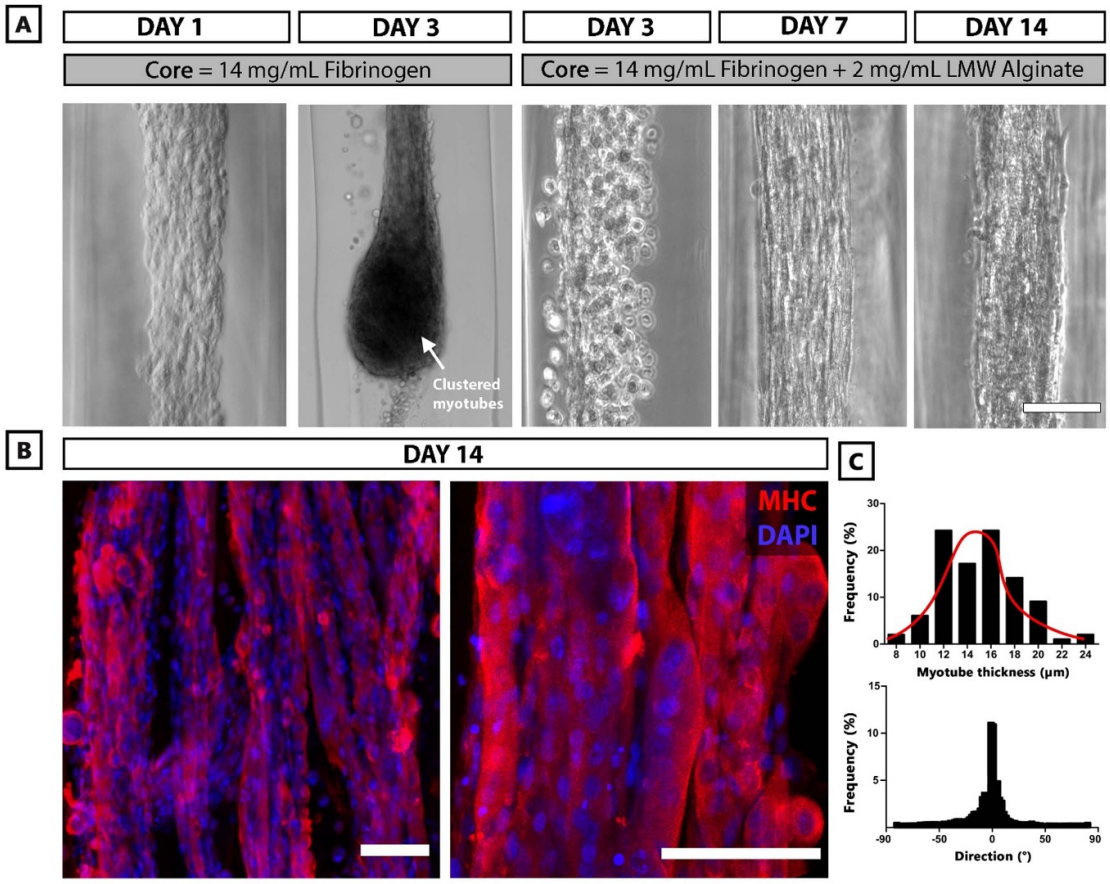

Figure 4. Engineered skeletal muscle constructs using 3D RoWS technique (A) bright-field micrographs of C2C12 during maturation in core/shell fibers at various time points and for two different core bioink compositions—14 mg ml^{-1} fibrinogen and 14 mg ml^{-1} fibrinogen + 2 mg ml^{-1} LMW alginate (scale bar: 150 μm) (B) confocal images of skeletal muscle constructs stained for MHC (red) and DAPI (blue) after 14 d of culture (core composition = 14 mg ml^{-1} fibrinogen + 2 mg ml^{-1} LMW alginate; left, 20X magnification, scale bar: 200 μm, right, 40X magnification, scale bar: 100 μm). (C) Myotube thickness directionality was assessed from MHC signal (0° corresponding to the fiber direction).

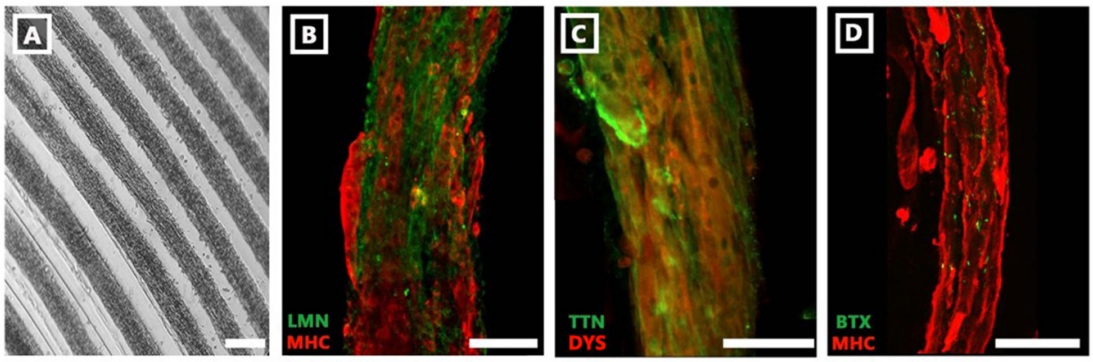

Figure 5. Expression of structural proteins within eSM bundles (A) bright-field micrographs of the volumetric fraction of the mature bundles at day 14 (scale bar: 500 μm), confocal images of eSM constructs stained for (B) laminin (green) and MHC (red), (C) titin (green) and dystrophin (red), (D) α-bungarotoxin (green) and MHC (red), after 14 d of culture (40X magnification, scale bars: 100 μm).

molecular level. In this regard, we speculate that the rapid extrusion process of the inks combined with an instantaneous crosslinking of the resulting core/shell fibers, the highly anisotropic architecture of the fibers, and shear-induced preferential organization of the core polymer chains induced a preferential alignment of the C2C12 cells along the extrusion direction, thus enhancing myofiber differentiation and maturation [8, 35] (figure 4(c)).

To better assess eSM bundle differentiation and maturation levels, we have performed a more detailed analysis of the obtained volumetric eSM bundles (figure 5(a)) against key markers, including laminin, titin, dystrophin, and acetylcholine

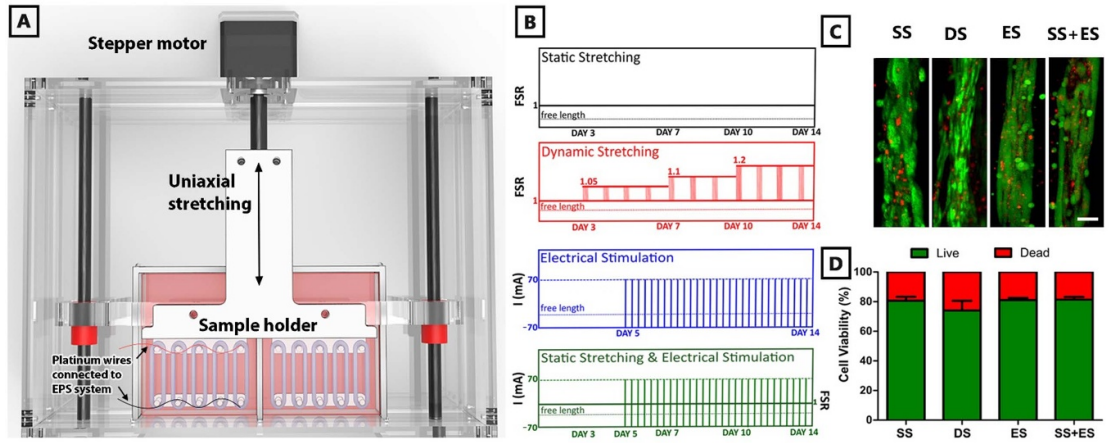

Figure 6. Physical stimulation of engineered muscle constructs. (A) 3D rendering of the custom electro-mechanical stimulation bioreactor for the simultaneous conditioning of up to 10 constructs. (B) The stimulation protocols employed to elicit skeletal muscle maturation (FSR—fiber stretching ratio—defined as stretched length over initial length of the fibers, I; applied current) (C) The effect of electro-mechanical stimulation on cell viability assessed on day 7 using a live/dead staining (scale bar: 50 μm) (D) Quantification of the cell viability from the confocal images shown in (c) (SS: static stretching, DS: dynamic stretching, ES: electrical stretching, SS + ES: static stretching + electrical stimulation).

receptors (AChRs, figures 5(b)–(d)). We specifically targeted these three proteins due to their crucial roles in maintaining the structural integrity, organization, and proper functioning of the SM structure. Moreover, they play a pivotal role in determining myofiber elasticity, passive tension, stiffness, and sarcomere stability during maturation [36, 37]. Along with the presence of the structural proteins, AChRs hold significant importance as AChR clustering is essential for correct neuromuscular signaling junction assembly and synaptic communication between motor neurons and muscle fibers. Using bungarotoxin staining, we have demonstrated the clustering and distribution of proper AChRs along the eSM bundles, providing further evidence of their maturation and functionality (figure 5(d)).

3.3. Influence of physical stimulation on muscle maturation and myosin heavy chain (MyH) isoform expression

Myogenic maturity, muscle mass, size, and functionality in SM are regulated by mechanical load and neuronal activity. Hence, for *in vitro* SM models, bioreactors incorporating miniaturized electro-mechanical stimulations are essential to investigate how different stimulations affect cell fates within fiber-shaped constructs. Accordingly, we have designed a bioreactor that can exert electrical and mechanical stimulations independently or simultaneously to the biofabricated SM bundles (figure 6(a), see SI for details). Specifically, mechanical stimulation is obtained through a linear stage controlled by a stepper motor, while ES is applied through a custom-made electrical pulse stimulation (EPS) system. Biofabricated SM bundles are mounted between the movable pins of a sample holder and rigid pins placed within the culture chamber. For ES, we used two platinum wires—each wrapped around a set of opposing pins—connected to the outputs of the EPS system.

Prior to the electro-mechanical stimulations, SM bundles were mounted on the opposing pins, and the distance between them was adjusted to exert a minimal pre-load on the samples. For our experiments, we selected four different stimulation protocols (SS, DS, ES, and SS + ES based on previously reported 3D muscle models (figure 6(b))) [3, 6, 17, 18]. For the SS protocol, the samples were placed in the bioreactor with a fixed distance between pillars for 14 d. The DS protocol progressively increased the stretching amplitude to compensate for sample relaxation. The stretching was applied at a specific speed and length on different days. Additionally, ES was introduced on day 5, consisting of a specific duration and amplitude of bipolar electrical impulses. Both stretching and ES were implemented simultaneously in the SS + ES protocol. The SS protocol was inspired by the vital low-level, passive tension of resistance to stretch. This passive tension for the physiological condition is termed the human resting muscle (myofascial) tone of SM that contributes to maintaining postural stability in balanced equilibrium positions while at rest [38]. Differently, the DS protocol aimed to investigate the maturation of the myobundles under periodical mechanical load with breaks at resting tone. The stretching/resting period and the amplitude of the mechanical stretching were

decided on the maximum period and the stretch to failure intensity from the works previously reported [6]. Additionally, we used cycles of ES to mimic the action potential generated by the central nervous system. As previously reported, the ES can increase myotube alignment and improve muscle maturity, myotube diameter, and tetanic force [16]. Hence, the sole electrical and ES combined with SS were tested to elicit muscle maturation. To confirm the cytocompatibility of the selected stimulation protocols on the engineered SM constructs, live–dead staining was performed on day 7. For all cases, cell viabilities were approx. 80% (SS $=$ 80 $\pm$ 4.5%, DS $=$ 74 $\pm$ 11%, ES $=$ 81 $\pm$ 3%, SS $+$ ES $=$ 81 $\pm$ 3%). Notably, the dominance of the viable and elongated myoblasts in each group indicates the suitability and properness of the amplitude and duration of the selected stimulation protocols (figures 6(c) and (d)).

To better understand myofiber maturation and the possible effect of electro-mechanical stimulation on the biofabricated samples, we decided to investigate the expression modulation of key gene markers related to various isoforms of MyH. Specifically, we studied the expression of MyH1, MyH2, and MyH7 genes. These three genes encode for the most abundant MHC isoforms in humans: MyH1 gene encodes for glycolytic, fast twitching type IIx fibers, MyH2 gene encodes for intermediate, fast oxidative type IIa fibers, and MyH7 encodes for oxidative, slow-twitching type I fibers [39]. The modulation of these genes is critical as the resulting properties of the engineered muscle constructs, such as energy consumption and contractile properties, strongly depend on MHC isoform content [4, 40–43].

The expression of the selected three MyH genes was analyzed at two time points—day 7 and day 14—, and their modulation was assessed with reference to the non-stimulated group (figures 7(a) and (b)). The stimulation protocols induced various modulations of the MyH isoforms. SS, for instance, resulted in an upregulation of all three MyH isoforms, with a slightly major effect on MyH1 at day 14. Contrarily, when the engineered SM constructs were subjected to the DS protocol, we found a significant upregulation of only MyH2 and minor effects over MyH1 and MyH7. This result is interesting and in line with the type of physical stimulation applied. In fact, MyH2 encodes for the MHC isoform contained in type IIa fibers (intermediate fibers) which are fast-twitching yet more fatigue-resistant than type IIx, being responsible in humans for activities such as walking where energy should be produced in a continuous and sustained manner. Notably, the electrically stimulated sample group (ES) revealed the highest upregulation of MyH1 among all studied groups, with minor effects over MyH2 and MyH7, indicating a MyH gene modulation towards the production of very fast twitching, glycolytic myofibers [44, 45]. Similarly, the combination of SS with ES resulted at day 14 in a major upregulation of MyH1 and a mild downregulation of MyH2 and MyH7. At first glance, the latter result may seem unexpected as both the SS and ES stimulation protocols, when applied singularly, had a positive upregulation effect—despite a different entity—over all three MyH genes. However, it clearly points out our partial understanding and knowledge of the complex network behind regulating these genes and, ultimately, how to control fiber maturation and type in engineered muscle constructs.

Along with the qRT-PCR analysis, we finally investigated myotube organization within the various experimental groups using immunofluorescence staining. As presented in figure 7(c), we found a homogeneous MHC expression in all groups accompanied by the formation of multi-nuclear, parallelly organized myotubes, thus indicating a proper myogenic differentiation. Nevertheless, we noticed distinct morphological differences in the samples treated with DS. In particular, despite a homogeneous expression of MHC, a significant part of myotubes appeared broken into shorter pieces. This aspect indicates that the applied amplitude and duration of the stretching may have resulted in the partial disruption of the forming neo-myotubes.

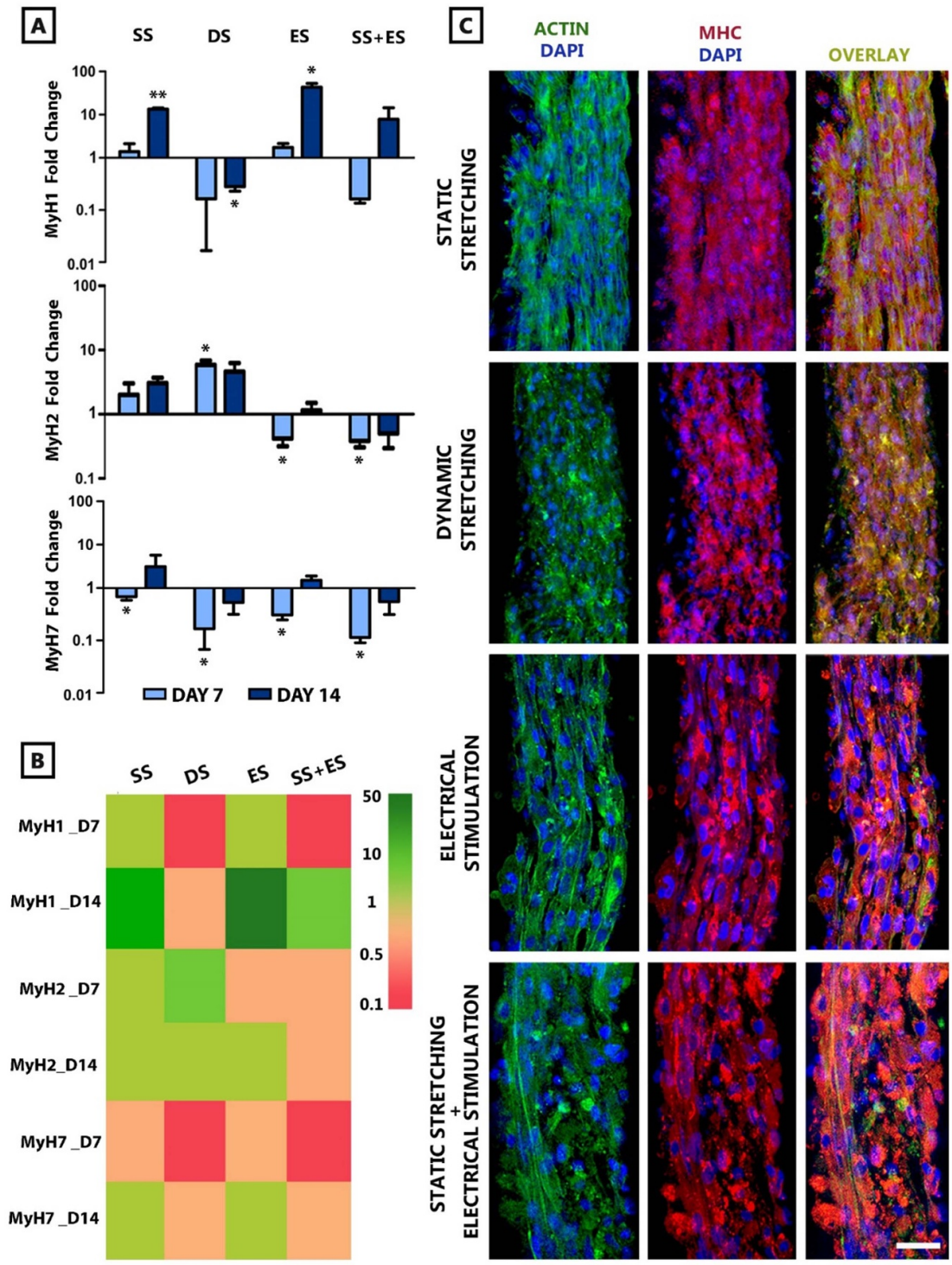

Figure 7. Modulation of myosin heavy chain isoforms in biofabricated SM constructs. (A) qRT-PCR data of MyH1, MyH2, and MyH7 isoforms on day 7 (light blue bars) and day 14 (dark blue bars) of culture. Significant differences are determined against non-stimulated conditions (free-floating samples) at corresponding timepoint: $^{*}p < 0.05$, $^{**}p < 0.01$) (B) A color-scale heat map summarizing the qRT-PCR of MyH1, MyH2, and MyH7. Red colors indicate downregulation; green colors indicate upregulation of genes. (C) Confocal images of physically stimulated myo-substitutes after 14 d of culture (actin (green), MHC (red), DAPI (blue), magnification: 20X, scale bars: 50 μm).

4. Conclusion

In this study, we have presented a new biofabrication strategy that harnesses wet-spinning principles to fabricate volumetric (approx. 0.5 ml min^{-1}) anisotropic 3D constructs composed of parallelly aligned, densely packed hydrogel fibers. The platform was tested in combination with a custom MPH that enabled the continuous fabrication of core/shell fibers. By tuning the chemical composition and mechanical stiffness of the two compartments of the fibers, we demonstrated that one could achieve a robust differentiation of SM

progenitors with the proper 3D organization of the neo-forming myotubes and expression of key marker proteins (MHC). Additionally, the presence of key structural proteins, along with the observed clustering of AChRs, indicated the potential responsiveness of our eSM bundles to physical stimulation, highlighting their capacity for functional activity. Further, the biofabricated eSM constructs were subjected to different electro-mechanical stimulation protocols to investigate possible modulation of various MHC isoform expressions (MyH1, MyH2, and MyH7). Such aspect is of the utmost importance as the overall contractile properties of the engineered muscles depend on their MHC isoform content, thus being critical in SMTE to design artificial muscles with specific biomimetic properties. Of note, the selected stimulation protocols had a different impact on the maturation of our samples with (i) a major overexpression of MyH1 in the case of ES, (ii) a major overexpression of MyH2 in the case of DS, and (iii) a combined overexpression of all three isoforms for SS. Altogether, the presented data shows that a more systematic screening of these input parameters, possibly combined with a functional analysis of the engineered SM contractile properties, should be performed in the future to better understand this intricate, still elusive biological process.

Data availability statement

The data that support the findings of this study are available upon reasonable request from the authors.

Acknowledgments

This study was supported by the National Science Centre Poland (NCN) within the SONATA 14 2018/31/D/ST8/03647 and PRELUDIUM 19 Project No. 2020/37/N/ST5/03272. This work was also supported by Research Projects CNR Progetti at CNR under the Grant No.: CUP: B93C20046330005. We would like to acknowledge Prof Fabio Domenici at Department of Chemical Science and Technologies, University of Rome "Tor Vergata", Rome, Italy for their support in confocal image acquisition.

Conflict of interest

The authors declare no competing interests.

ORCID iDs

Nehar Celikkin https://orcid.org/0000-0001-8858-2057
Agnieszka Wiśniewska https://orcid.org/0000-0001-5317-757X
Chiara Rinoldi https://orcid.org/0000-0002-4028-375X
Marco Costantini https://orcid.org/0000-0003-2756-5872

References

[1] Frontera W R and Ochala J 2015 Skeletal muscle: a brief review of structure and function *Calcif. Tissue Int.* **96** 183–95
[2] Jabre S, Hleihel W and Coirault C 2021 Nuclear mechanotransduction in skeletal muscle *Cells* **10** 1–18
[3] Ashida Y, Himori K, Tatebayashi D, Yamada R, Ogasawara R and Yamada T 2018 Effects of contraction mode and stimulation frequency on electrical stimulation-induced skeletal muscle hypertrophy *J. Appl. Physiol.* **124** 341–8
[4] Ganassi M, Badodi S, Wanders K, Zammit P S and Hughes S M 2020 Myogenin is an essential regulator of adult myofibre growth and muscle stem cell homeostasis *eLife* **9** 1–23
[5] Juan L, Saul D, Böker K O, Ernst J, Lehman W and Schilling A F 2018 Current methods for skeletal muscle tissue repair and regeneration *Biomed Res. Int.* **2018** 11
[6] Heher P, Maleiner B, Prüller J, Teuschl A H, Kollmitzer J, Monforte X, Wolbank S, Redl H, Rünzler D and Fuchs C 2015 A novel bioreactor for the generation of highly aligned 3D skeletal muscle-like constructs through orientation of fibrin via application of static strain *Acta Biomater.* **24** 251–65
[7] Rangarajan S, Madden L and Bursac N 2014 Use of flow, electrical, and mechanical stimulation to promote engineering of striated muscles *Ann. Biomed. Eng.* **42** 1391–405
[8] Costantini M, Testa S, Fornetti E, Fuoco C, Sanchez Riera C, Nie M, Bernardini S, Rainer A, Baldi J and Zoccali C 2021 Biofabricating murine and human myo-substitutes for rapid volumetric muscle loss restoration *EMBO Mol. Med.* **13** e12778
[9] Dessauge F, Schleder C, Perruchot M-H and Rouger K 2021 3D *in vitro* models of skeletal muscle: myopshere, myobundle and bioprinted muscle construct *Vet. Res.* **52** 1–12
[10] Cheng D and Chen F-E 2020 Experimental and numerical studies of the phase-transfer-catalyzed Wittig reaction in liquid–liquid slug-flow microchannels *Ind. Eng. Chem. Res.* **59** 4397–410
[11] Huang Y C, Dennis R G and Baar K 2006 Cultured slow vs. fast skeletal muscle cells differ in physiology and responsiveness to stimulation *Am. J. Physiol., Cell Physiol.* **291** 11–17
[12] Jodat Y A, Kiaee K, Vela Jarquin D, la Garza Hernández R L D, Wang T, Joshi S, Rezaei Z, de Melo B A G, Ge D and Mannoor M S 2020 A 3D-printed hybrid nasal cartilage with functional electronic olfaction *Adv. Sci.* **7** 1901878
[13] Tarum J, Folkesson M, Atherton P J and Kadi F 2017 Electrical pulse stimulation: an *in vitro* exercise model for the induction of human skeletal muscle cell hypertrophy. A proof-of-concept study *Exp. Physiol.* **102** 1405–13
[14] Khodabukus A, Madden L, Prabhu N K, Koves T R, Jackman C P, Muoio D M and Bursac N 2019 Electrical stimulation increases hypertrophy and metabolic flux in tissue-engineered human skeletal muscle *Biomaterials* **198** 259–69
[15] Zhuang P, An J, Chua C K and Tan L P 2020 Bioprinting of 3D *in vitro* skeletal muscle models: a review *Mater. Des.* **193** 108794
[16] Wang J, Khodabukus A, Rao L, Vandusen K, Abutaleb N and Bursac N 2019 Engineered skeletal muscles for disease modeling and drug discovery *Biomaterials* **221** 119416
[17] Boonen K J M, Langelaan M L P, Polak R B, van der Schaft D W J, Baaijens F P T and Post M J 2010 Effects of a combined mechanical stimulation protocol: value for skeletal muscle tissue engineering *J. Biomech.* **43** 1514–21
[18] Chen X, Du W, Cai Z, Ji S, Dwivedi M, Chen J, Zhao G and Chu J 2020 Uniaxial stretching of cell-laden microfibers for promoting C2C12 myoblasts alignment and myofibers formation *ACS Appl. Mater. Interfaces* **12** 2162–70

[19] Mazari-Arrighi E, Okitsu T, Teramae H, Aoyagi H, Kiyosawa M, Yano M, Chatelain F, Fuchs A and Takeuchi S 2022 *In vitro* proliferation and long-term preservation of functional primary rat hepatocytes in cell fibers *Sci. Rep.* **12** 1–12
[20] Shima A, Itou A and Takeuchi S 2020 Cell fibers promote proliferation of co-cultured cells on a dish *Sci. Rep.* **10** 1–7
[21] van Genderen A M, Valverde M G, Capendale P E, Kersten V, Garví E S, Schuurmans C C L, Ruelas M, Soeiro J T, Tang G and Janssen M J 2022 Co-axial printing of convoluted proximal tubule for kidney disease modeling *Biofabrication* **14** 044102
[22] Onoe H and Takeuchi S 2012 Tublogenesis of endothelial cells in core-shell hydrogel microfibers *16th Int. Conf. on Miniaturized Systems for Chemistry and Life Sciences, MicroTAS 2012* (Chemical and Biological Microsystems Society) pp 1069–71
[23] du Chatinier D N, Figler K P, Agrawal P, Liu W and Zhang Y S 2021 The potential of microfluidics-enhanced extrusion bioprinting *Biomicrofluidics* **15** 41304
[24] Yang G H, Kang D, An S, Ryu J Y, Lee K, Kim J S, Song M-Y, Kim Y-S, Kwon S-M and Jung W-K 2022 Advances in the development of tubular structures using extrusion-based 3D cell-printing technology for vascular tissue regenerative applications *Biomater. Res.* **26** 1–13
[25] Dang T T, Hwang C H, Back S H and Koo K 2020 Coaxial printing of double-layered and free-standing blood vessel analogues without ultraviolet illumination for high-volume vascularised tissue *Biofabrication* **12** 45033
[26] Onoe H, Okitsu T, Itou A, Kato-Negishi M, Gojo R, Kiriya D, Sato K, Miura S, Iwanaga S and Kuribayashi-Shigetomi K 2013 Metre-long cell-laden microfibres exhibit tissue morphologies and functions *Nat. Mater.* **12** 584–90
[27] Costantini M *et al* 2017 Microfluidic-enhanced 3D bioprinting of aligned myoblast-laden hydrogels leads to functionally organized myofibers *in vitro* and *in vivo* *Biomaterials* **131** 98–110
[28] Mueller C, Trujillo-Miranda M, Maier M, Heath D E, O'Connor A J and Salehi S 2021 Effects of external stimulators on engineered skeletal muscle tissue maturation *Adv. Mater. Interfaces* **8** 2001167
[29] Gilbert P M, Havenstrite K L, Magnusson K E G, Sacco A, Leonardi N A, Kraft P, Nguyen N K, Thrun S, Lutolf M P and Blau H M 2010 Substrate elasticity regulates skeletal muscle stem cell self-renewal in culture *Science* **329** 1078–81
[30] Salinas C N and Anseth K S 2008 The influence of the RGD peptide motif and its contextual presentation in PEG gels on human mesenchymal stem cell viability *J. Tissue Eng. Regen. Med.* **2** 296–304
[31] Kim M H and Lin C-C 2023 Poly (ethylene glycol)–norbornene as a photoclick bioink for digital light processing 3D bioprinting *ACS Appl. Mater. Interfaces* **15** 2737–46
[32] Barbosa M and Martins M C L 2017 *Peptides and Proteins as Biomaterials for Tissue Regeneration and Repair* (Woodhead Publishing)
[33] Campbell P G, Durham S K, Hayes J D, Suwanichkul A and Powell D R 1999 Insulin-like growth factor-binding protein-3 binds fibrinogen and fibrin *J. Biol. Chem.* **274** 30215–21
[34] Sahni A, Odrljin T and Francis C W 1998 Binding of basic fibroblast growth factor to fibrinogen and fibrin *J. Biol. Chem.* **273** 7554–9
[35] Kim J H, Seol Y-J-J, Ko I K, Kang H-W-W, Lee Y K, Yoo J J, Atala A and Lee S J 2018 3D bioprinted human skeletal muscle constructs for muscle function restoration *Sci. Rep.* **8** 1–15
[36] van Ry P M, Minogue P, Hodges B L and Burkin D J 2014 Laminin-111 improves muscle repair in a mouse model of merosin-deficient congenital muscular dystrophy *Hum. Mol. Genet.* **23** 383–96
[37] Petrof B J, Shrager J B, Stedman H H, Kelly A M and Sweeney H L 1993 Dystrophin protects the sarcolemma from stresses developed during muscle contraction *Proc. Natl Acad. Sci.* **90** 3710–4
[38] Masi A T and Hannon J C 2008 Human resting muscle tone (HRMT): narrative introduction and modern concepts *J. Bodyw. Mov. Ther.* **12** 320–32
[39] Pette D and S S R 2000 Myosin isoforms, muscle fiber types, and transitions *Microsc. Res. Tech.* **50** 500–9
[40] Schiaffino S and Reggiani C 2011 Fiber types in mammalian skeletal muscles *Physiol. Rev.* **91** 1447–531
[41] Gejl K D, Hvid L G, Andersson E P, Jensen R, Holmberg H-C and Ørtenblad N 2021 Contractile properties of MHC I and II fibers from highly trained arm and leg muscles of cross-country skiers *Front. Physiol.* **12** 855
[42] Ausoni S, Gorza L, Schiaffino S, Gundersen K and Lomo T 1990 Expression of myosin heavy chain isoforms in stimulated fast and slow rat muscles *J. Neurosci.* **10** 153–60
[43] Tajsharghi H, Darin N, Rekabdar E, Kyllerman M, Wahlström J, Martinsson T and Oldfors A 2005 Mutations and sequence variation in the human myosin heavy chain IIa gene (MYH2) *Eur. J. Hum. Genet.* **13** 617–22
[44] Vissing K, Andersen J L, Harridge S D R, Sandri C, Hartkopp A, Kjaer M and Schjerling P 2005 Gene expression of myogenic factors and phenotype-specific markers in electrically stimulated muscle of paraplegics *J. Appl. Physiol.* **99** 164–72
[45] Khodabukus A, Baehr L M, Bodine S C and Baar K 2015 Role of contraction duration in inducing fast-to-slow contractile and metabolic protein and functional changes in engineered muscle *J. Cell. Physiol.* **230** 2489–97